Engineering Analysis with Boundary Elements 36 (2012) 1151–1163

Contents lists available at SciVerse ScienceDirect

Engineering Analysis with Boundary Elements

journal homepage: www.elsevier.com/locate/enganabound

A fully nonlinear implicit model for wave interactions with submerged structures in forced or free motion

Etienne Guerber [a,*], Michel Benoit [a], Stephan T. Grilli [b], Clément Buvat [a]

[a] Saint-Venant Laboratory for Hydraulics, Université Paris-Est (Joint Research Unit Between EDF R&D, CETMEF and Ecole des Ponts Paris-Tech), 6 quai Watier, BP 49, 78401 Chatou Cedex, France

[b] Department of Ocean Engineering, University of Rhode Island, Narragansett, 04282 RI, USA

ARTICLE INFO

Article history:
Received 8 June 2011
Accepted 9 February 2012

Keywords:
Nonlinear waves
Boundary Element Method
Numerical Wave Tank
Wave–structure interactions
Wave Energy Converter (WEC)

ABSTRACT

The purpose of this work is to develop advanced numerical tools for modeling two-way fully nonlinear interactions of ocean surface waves (irregular waves in the general situation) with submerged structures undergoing large amplitude motion, that could represent Wave Energy Converters (WECs). In our modeling approach, an existing two-dimensional Numerical Wave Tank (NWT), based on potential flow theory, is extended to include a submerged horizontal cylinder of arbitrary cross-section. The mathematical problem and related numerical solution are first introduced. Then, conservation of volume and conservation of energy are checked, respectively, in the case of a circular cylinder in a prescribed large amplitude motion and in the case of a circular cylinder in a free motion. Interactions between waves and a submerged circular cylinder computed by the model are then compared to mathematical solutions for two situations: a cylinder in prescribed motion and a freely moving cylinder.

1. Introduction

In recent years there has been a renewed interest in using ocean renewable energy and, in particular, wave energy. To do so, many types of Wave Energy Converters (WECs) have been proposed, and some were constructed and tested. The so-called point-absorbers are a class of WECs that harvest the wave-induced motion of oscillating submerged bodies (see, e.g., the CETO system [1]). Such bodies can be located quite close to the free surface and hence may undergo large amplitude motion. In these situations numerical models based on assuming small amplitude motions, either of the free surface elevation, the body dynamics, or both, may not properly represent the dynamics of the coupled system. In the present study, we develop and implement a numerical model, solving two-way nonlinear wave–body interactions, which could then be applied to simulating WEC behavior in real (irregular) sea-states. As a first step in this project, we implement and validate a two-dimensional (2D) model for a horizontal submerged cylinder of arbitrary cross-section. Future work will report on the three-dimensional implementation of this model and its application to more realistic submerged bodies.

Many papers have been dedicated to the analytical, numerical and experimental study of the nonlinear response of submerged circular cylinders. Chaplin [2], for instance, experimentally studied in a wave tank the influence of the Keulegan–Carpenter number on the nonlinear wave force applied to a fixed submerged cylinder. More recently, Wu [3] formulated a mathematical model to calculate the forces exerted on a submerged cylinder undergoing large-amplitude motions. In [3], the no-flow boundary condition on the submerged body was satisfied on its instantaneous position, while the free surface condition was linearized. The solution for the velocity potential is expressed in terms of a multipole expansion. In particular, Wu obtained results for a circular cylinder in prescribed motion in a wave field: purely vertical motion and clock-wise circular motion [3]. Such studies were later used to validate results of numerical models based on potential flow theory. Among others, Cointe [4] compared numerical results from his Fully Nonlinear Potential FLow (FNPF) model to Chaplin's experiments. Kent and Choi [5] used a High-Order Spectral Method (HOS) and compared their results to both Wu's theory and Chaplin's experiments. Koo and Kim [6,7] used a 2D Numerical Wave Tank (NWT) to study fully nonlinear wave–body interactions for various surface piercing bodies. They used the method of the acceleration potential introduced by Tanizawa [8] to compute the time derivative of the potential $\partial\phi/\partial t$ (this is detailed later). This method has also been applied by Sung and Choi [9] to compute the nonlinear radiation of water waves by a surface piercing body and by Yim and Tanizawa [10], who

* Corresponding author. Tel.: +33 130877970; fax: +33 130878086.
E-mail addresses: etienne.guerber@edf.fr (E. Guerber), michel.benoit@edf.fr (M. Benoit), grilli@oce.uri.edu (S.T. Grilli), grilli@oce.uri.edu (C. Buvat).

0955-7997/$ - see front matter © 2012 Elsevier Ltd. All rights reserved.
doi:10.1016/j.enganabound.2012.02.005

compared results from their 2D-FNPF model to experiments performed on a moored submerged sphere, subjected to waves. In their 2DV simulations, the sphere is converted to an equivalent horizontal cylinder. Other numerical tools based on the Finite Element Method (FEM) to solve the Navier–Stokes equations were used for example by Tavassoli and Kim [11,12] to analyze the interactions between nonlinear waves and a circular cylinder in a viscous 2D-NWT.

The numerical simulations reported here are also performed using a 2D-FNPF model, which is an extension of Grilli et al.'s Boundary Element Model (BEM) code, developed over the past 20 years to simulate processes of wave generation, propagation and interaction with structures, and dissipation through breaking or absorption in a numerical beach (e.g., [13–15]). The latter processes take place both in the field and laboratory tanks; this has led such models to be referred to as Numerical Wave Tanks (NWTs). Specifically, we use the NWT to simulate strongly nonlinear interactions (i.e., induced motions and forces) between wave-induced flows and a submerged body representing a WEC section, slackly moored on the ocean bottom. To achieve high accuracy of the solution and thus to perform long term simulations without need for smoothing or filtering of the solution, we use higher order boundary elements and very accurate numerical integration methods. An absorbing beach combining an "absorbing pressure" on the free surface and a lateral absorbing piston wavemaker allows to achieve negligible reflection in the NWT. Various ways of generating waves are available, including flap or piston wavemakers, and exact nonlinear waves (both periodic streamfunction waves, and solitary waves). Wavemakers can also be used to generate nonlinear random waves, based on a specified energy spectrum. A feedback control loop allows to iteratively modify the wavemaker stroke spectrum to obtain an accurate realization of the target wave spectrum. While random waves can be generated, the present work, which is aimed at establishing the overall properties of convergence and accuracy of the model, focuses on nonlinear interactions of a cylindrical structure with monochromatic periodic waves.

Second-order Taylor series expansions, expressed in an Eulerian–Lagrangian formulation, are used to update the free surface potential and elevation to the next time step, as well as the position of the absorbing wavemaker at the far end of the NWT. This requires solving two BEM problems at each time step, one for the potential and one for its time derivative (the latter allows for a straightforward calculation of pressure on all boundaries, including on the submerged structure/WEC). In the case of freely moving bodies, the specification of the time derivative of the potential on the body surface, requires solving an additional Boundary Integral Equation (BIE). This is done using the so-called *implicit method* introduced by Van Daalen [16], which is similar to the *acceleration potential* method of Tanizawa [8]. This method is very effective since both body motion and adjacent fluid velocity are simultaneously solved [8,6].

In the remainder of this paper, we first present in Section 2 the mathematical formulation of the model and then in Section 3 its numerical implementation. This is followed in Section 4 by a comprehensive assessment of the model convergence and accuracy, by analyzing errors on energy and mass conservation for a series of applications, as compared to a reference solution. Section 5 presents more realistic simulations, where numerical results are compared to theoretical results.

2. Mathematical formulation

Equations for the two-dimensional FNPF model are briefly presented in the following (see [13–15,17] for details).

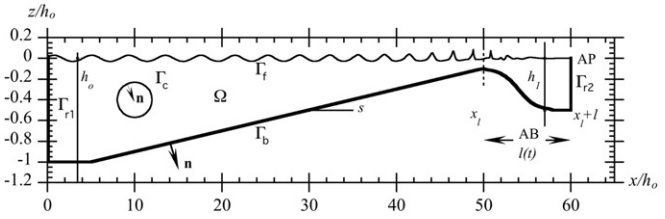

Fig. 1. Sketch of computational domain Ω of 2D-NWT, and its boundaries.

2.1. Hydrodynamic model

The velocity potential $\phi(\boldsymbol{x},t)$ is used to describe the irrotational flow of an inviscid fluid in the vertical plane (x,z) and the velocity is defined by $\boldsymbol{u} \equiv (u,w) = \nabla\phi$. Mass conservation in the fluid domain $\Omega(t)$, with boundary $\Gamma(t)$, is expressed as a Laplace's equation for the potential (Fig. 1)

$$\Delta\phi = 0 \quad \text{in } \Omega(t) \tag{1}$$

From this equation, a second Laplace's equation is easily derived for the time derivative of the potential $\phi_t \equiv \partial\phi/\partial t$

$$\Delta\phi_t = 0 \quad \text{in } \Omega(t) \tag{2}$$

As will appear later, accurate values of ϕ_t are needed both to compute second-order terms in the time-integration of the free surface boundary geometry and potential, and for specifying boundary conditions on submerged moving bodies. In the former, using ϕ_t and its spatial derivatives ensures a higher accuracy and stability, thereby eliminating the need for filtering or smoothing on the free surface. In the latter, ϕ_t allows computing the pressure p along the body boundary $\Gamma_c(t)$, which depends on ϕ_t. As will be detailed later, this is key to dealing with freely moving bodies with high amplitude motion. As reported by several authors (e.g., [4,6]), using backward finite difference schemes to compute ϕ_t is not sufficiently accurate and leads to numerical instabilities. The solution of Laplace's equations (1) and (2) requires well-posed Dirichlet–Neumann boundary conditions, which are detailed in the next subsections. Note, for simplicity, in the following, all partial derivatives of the potential will be indicated by subscripts. For example, ϕ_n will stand for $\partial\phi/\partial n \equiv \nabla\phi \cdot \boldsymbol{n}$ and ϕ_{tn} for $\partial^2\phi/\partial t\partial n$.

2.2. Free surface boundary conditions

On the free surface $\Gamma_f(t)$, ϕ satisfies the kinematic and dynamic boundary conditions

$$\frac{D\boldsymbol{r}}{Dt} = \left(\frac{\partial}{\partial t} + \boldsymbol{u}\cdot\nabla\right)\boldsymbol{r} = \boldsymbol{u} = \nabla\phi \quad \text{on } \Gamma_f(t) \tag{3}$$

$$\frac{D\phi}{Dt} = -gz + \frac{1}{2}\nabla\phi\cdot\nabla\phi - \frac{p_a}{\rho} \quad \text{on } \Gamma_f(t) \tag{4}$$

respectively, with $\boldsymbol{r} = (x,z)$, the position vector on the free surface, g the gravitational acceleration, z the vertical coordinate, p_a the atmospheric pressure at the free surface, and ρ the fluid density. Using Eqs. (3) and (4) to integrate in time the free surface position and the free surface potential ϕ^f, a Dirichlet boundary condition on $\Gamma_f(t)$ can be specified for the Laplace problem (1) for ϕ

$$\phi = \phi^f \quad \text{on } \Gamma_f(t) \tag{5}$$

Once the latter is solved, Eq. (4) yields a Dirichlet boundary condition on $\Gamma_f(t)$ for the Laplace problem (2) for ϕ_t

$$\phi_t = \phi_t^f = -gz - \frac{1}{2}\nabla\phi\cdot\nabla\phi - \frac{p_a}{\rho} \quad \text{on } \Gamma_f(t) \tag{6}$$

2.3. Bottom and lateral boundary conditions

Along the stationary bottom Γ_b, a no-flow condition is prescribed as a homogeneous Neumann condition for both problems for ϕ and ϕ_t

$$\phi_n = 0 \quad \text{and} \quad \phi_{tn} = 0 \quad \text{on } \Gamma_b \tag{7}$$

On the leftward boundary of the NWT, Γ_{r1}, periodic or irregular waves are generated by an oscillating piston or flap wavemaker. An exact wave generation for periodic progressive waves, based on the stream-function wave theory, can also be specified, together with a zero-mass flux condition [15]. On the rightward side of the tank, an absorbing beach (AB) is implemented to reduce wave reflection from the far end boundary Γ_{r2}. More precisely, an artificial counteracting pressure is applied over a given distance in the dynamic free surface condition (Eq. (4)), which creates a negative work against incident waves. In addition, a piston-like absorbing boundary condition, first introduced by Clément [18], is specified on boundary Γ_{r2}. These methods of generation and absorption of waves lead to Dirichlet or Neumann boundary conditions for the two Laplace problems that will not be detailed in the present article. For more information, see Grilli and Horrillo [15].

2.4. Body boundary conditions

The 2D-NWT originally developed by Grilli et al. was modified to include totally submerged rigid bodies, under the free surface. Two situations were successively considered, the case of a body: (i) in prescribed motion (including the case of a fixed body) and (ii) undergoing "free" motion (under the effects of various forces applied to it). Boundary conditions for each case are detailed next.

2.4.1. Body in prescribed motion

When the body motion is specified, the boundary condition on the body surface is simply expressed as a Neumann condition for the potential

$$\phi_n = \dot{\boldsymbol{x}} \cdot \boldsymbol{n} \quad \text{on } \Gamma_c(t) \tag{8}$$

where $\dot{\boldsymbol{x}}$ is the velocity for points on the body boundary, which is known when the motion of the body is prescribed.

Another Neumann condition for ϕ_{tn} is specified on the body boundary, to solve for ϕ_t. Following Cointe [4], Grilli and Svendsen [17], Van Daalen [16], or Tanizawa [8], this reads as

$$\phi_{tn} = \ddot{\boldsymbol{x}} \cdot \boldsymbol{n} + v(\boldsymbol{x}) \quad \text{on } \Gamma_c(t) \tag{9}$$

with v, a local quantity defined at point $\boldsymbol{x}$ of the body boundary $\Gamma_c(t)$, expressed here for 2D problems as

$$v(\boldsymbol{x}) = (\dot{\boldsymbol{x}} \cdot \boldsymbol{s} - \phi_s)\dot{\theta}_G - \left(\frac{1}{R}\phi_s + \phi_{sn}\right)\dot{\boldsymbol{x}} \cdot \boldsymbol{s} + \left(\phi_{ss} - \frac{1}{R}\phi_n\right)\dot{\boldsymbol{x}} \cdot \boldsymbol{n} \tag{10}$$

where $1/R$ is the local curvature of the boundary, $\boldsymbol{n}$ and $\boldsymbol{s}$ are the local normal and tangential vectors, $\ddot{\boldsymbol{x}}$ and $\dot{\theta}_G$ are the body acceleration and angular velocity with respect to the center of mass G, respectively. Boundary conditions (Eqs. (8) and (9)) are similar to the boundary conditions specified for the generation of waves by a flap-type wavemaker [19,15]. Various results will be presented in Sections 4.1 and 5.1, for a submerged circular cylinder in forced vertical motion.

2.4.2. Freely moving body

This is the case of a loosely tethered or slackly moored submerged body subjected to wave action. In this case, the body kinematics needed in Eqs. (8)–(10) is not *a priori* known. Hence, $\dot{\boldsymbol{x}}$, $\ddot{\boldsymbol{x}}$ and $\dot{\boldsymbol{\theta}}_G$ must be computed by solving a coupled fluid–structure interaction problem, in which equations for the fluid and body motion are simultaneously solved. In this case, Eq. (9) also cannot be directly used as an explicit boundary condition to solve the Laplace problem for ϕ_t, but first needs to be formulated differently.

Assuming a body of mass M and moment of inertia I about its center of mass G, the dynamic equations governing body motion read as

$$M\ddot{\boldsymbol{x}}_G = \int_{\Gamma_c} p\boldsymbol{n}\, \mathrm{d}\Gamma + M\boldsymbol{g} + \boldsymbol{F}_{ext} \tag{11}$$

$$I\ddot{\boldsymbol{\theta}}_G = \int_{\Gamma_c} p(\boldsymbol{r} \times \boldsymbol{n})\, \mathrm{d}\Gamma + \boldsymbol{M}_{ext} \tag{12}$$

where $\ddot{\boldsymbol{x}}_G$ is the body center of mass acceleration, $\boldsymbol{F}_{ext}$ is the resultant of applied external forces, which essentially damp body motion (e.g., viscous drag, mooring and power take-off), $\boldsymbol{M}_{ext}$ the resulting moment of those forces about the center of mass, and $\boldsymbol{r}$ is the position of a point on the body boundary with respect to the center of mass. Finally, in these equations, pressure p along the body boundary is given by the (nonlinear) Bernoulli equation

$$p = -\rho(\phi_t + \tfrac{1}{2}\nabla\phi \cdot \nabla\phi + gz) \tag{13}$$

The main difficulty for computing this pressure is that both ϕ_t and ϕ_{tn} are unknown at any given time along $\Gamma_c(t)$, since these depend on body motion. Several strategies have been proposed to overcome this difficulty: (i) a mode decomposition method first proposed by Vinje and Brevig [20] and then used by, e.g., Cointe [4] and Koo and Kim [6]; (ii) the iterative method of Sen [21] and Cao et al. [22]; (iii) the indirect method of Wu and Eatock-Taylor [23]; and (iv) the implicit method of Van Daalen [16] and Tanizawa [8].

The implicit method is selected here, as it does not require iterations and there is no need to introduce any artificial potential. The principle of it is to express an additional relation between ϕ_t and ϕ_{tn} along $\Gamma_c(t)$, on the basis of the rigid body kinematics, which provides a relationship between $\ddot{\boldsymbol{x}}$, $\ddot{\boldsymbol{x}}_G$ and $\ddot{\boldsymbol{\theta}}_G$

$$\ddot{\boldsymbol{x}} = \ddot{\boldsymbol{x}}_G + \ddot{\boldsymbol{\theta}}_G \times \boldsymbol{r}(\boldsymbol{x}) + \dot{\boldsymbol{\theta}}_G \times (\dot{\boldsymbol{\theta}}_G \times \boldsymbol{r}(\boldsymbol{x})) \tag{14}$$

Replacing $\ddot{\boldsymbol{x}}$ from Eq. (14) into Eq. (9), and p from Eq. (13) in Eqs. (11) and (12), Van Daalen and Tanizawa both derived a similar BIE on $\Gamma_c(t)$

$$\phi_{tn}(\boldsymbol{x}) + \int_{\Gamma_c} K(\boldsymbol{x},\boldsymbol{\xi})\phi_t(\xi)\, d\Gamma_\xi = \gamma(\boldsymbol{x}) \quad \text{on } \Gamma_c(t) \tag{15}$$

in which the kernel function $K(\boldsymbol{x},\boldsymbol{\xi})$ is regular and symmetric and only depends on the rigid body geometry (i.e., is valid for all times)

$$K(\boldsymbol{x},\boldsymbol{\xi}) = \frac{1}{M}\boldsymbol{n}(\boldsymbol{x}) \cdot \boldsymbol{n}(\boldsymbol{\xi}) + \frac{1}{I}(\boldsymbol{r}(\boldsymbol{x}) \times \boldsymbol{n}(\boldsymbol{x})) \cdot (\boldsymbol{r}(\boldsymbol{\xi}) \times \boldsymbol{n}(\boldsymbol{\xi})) \tag{16}$$

and

$$\begin{aligned}\gamma(\boldsymbol{x}) = &-\int_{\Gamma_c}\left\{\frac{1}{2}\nabla\phi(\xi) \cdot \nabla\phi(\xi) + gz(\xi)\right\}K(\boldsymbol{x},\boldsymbol{\xi})\, d\Gamma_\xi \\ &-(\dot{\boldsymbol{\theta}}_G \cdot \dot{\boldsymbol{\theta}}_G)\boldsymbol{r}(\boldsymbol{x}) \cdot \boldsymbol{n}(\boldsymbol{x}) + v(\boldsymbol{x}) + \boldsymbol{g} \cdot \boldsymbol{n}(\boldsymbol{x}) \\ &-\frac{1}{M}\boldsymbol{F}_{ext} \cdot \boldsymbol{n}(\boldsymbol{x}) + \frac{1}{I}\boldsymbol{M}_{ext} \cdot (\boldsymbol{r}(\boldsymbol{x}) \times \boldsymbol{n}(\boldsymbol{x}))\end{aligned} \tag{17}$$

Eqs. (11)–(17) are the governing equations off a freely moving body, totally of partially submerged under the free surface.

2.5. Intermediate conclusions

Whether the submerged body undergoes a specified or free motion, the Laplace problem for ϕ has complete boundary conditions, using Eq. (5), (7) and (8) on $\Gamma_f(t)$, Γ_b and $\Gamma_c(t)$, respectively. Details of boundary conditions used for wave generation and absorption on Γ_{r1} and Γ_{r2} can be found in [15]. When the motion of the submerged body is specified, the Laplace

problem for ϕ_t has complete boundary conditions, using Eqs. (6), (7) and (9) on $\Gamma_f(t)$, Γ_b and $\Gamma_c(t)$, respectively. However, when the body is freely moving, Eq. (9) cannot be used on $\Gamma_c(t)$. Instead, the BIE (15) is used, which yields a mathematically well-posed Laplace problem for ϕ_t.

3. Numerical implementation

Both Laplace problems, discussed above, are solved at any given time t using a BEM in domain geometry $\Omega(t)$. Given such a solution, both domain geometry and boundary conditions are then updated to time $t+\Delta t$, where Δt denotes a small time step. Specifically, time updating involves:

- for the fluid: the free surface elevation and potential, and the lateral boundaries geometry and kinematics (e.g., generating and absorbing wavemakers),
- for the rigid submerged body: the position (defined by that of its center of mass and angle of rotation around the latter) and velocity of BEM nodes distributed along its boundary.

The updated positions of various boundaries thus define a new geometry $\Omega(t+\Delta t)$ for the fluid domain. The three next subsections briefly describe the numerical solution of the Laplace problems, the time updating of the free surface, and that of the freely moving body.

3.1. Numerical solution of Laplace problems for ϕ and ϕ_t

Green's second identity is applied to transform Eqs. (1) and (2) into BIEs, which are solved by a BEM. Thus, for a set of N discretization nodes $\boldsymbol{x}_l$ on boundary Γ

$$\alpha(\boldsymbol{x}_l)u(\boldsymbol{x}_l)=\int_{\Gamma_n}\left[\frac{\overline{\partial u}}{\partial n}G-u\frac{\partial G}{\partial n}\right]d\Gamma+\int_{\Gamma_d}\left[\frac{\partial u}{\partial n}G-\overline{u}\frac{\partial G}{\partial n}\right]d\Gamma,\quad l=1,\ldots,N \tag{18}$$

with u denoting either the unknown ϕ or ϕ_t values, and $\overline{u}$,$\overline{\partial u/\partial n}$, values prescribed by the boundary conditions. Γ_n refers to all boundary sections where $\overline{\partial u/\partial n}$ is specified (Neumann conditions), Γ_d to all boundary sections where $\overline{u}$ is specified (Dirichlet conditions), and $\alpha(\boldsymbol{x}_l)$ is a geometric coefficient. We denote by $G\equiv G(\boldsymbol{x},\boldsymbol{x}_l)$ the free space Green's function of Laplace's equation in 2D

$$G=-\frac{1}{2\pi}\ln r$$

$$\frac{\partial G}{\partial n}=-\frac{1}{2\pi}\frac{\boldsymbol{r}\cdot\boldsymbol{n}}{r^2} \tag{19}$$

with $r=|\boldsymbol{r}|=|\boldsymbol{x}-\boldsymbol{x}_l|$ the distance from the integration point $\boldsymbol{x}$ to the collocation point $\boldsymbol{x}_l$. Eq. (18) are then solved by the BEM, successively for ϕ and ϕ_t. To do so, various integrals are discretized by defining M higher order elements to interpolate in between discretization nodes. In the present applications, quadratic isoparametric elements are used on lateral, bottom, and body boundaries. Cubic elements are used on the free surface. In order to ensure continuity of the surface slope, in these so-called Mixed Cubic Interpolation (MCI) elements, geometry is modeled by cubic splines and field variables are interpolated between each pair of nodes, using the mid-section of a four-node "sliding" isoparametric element. Expressions of BEM integrals (regular, singular, quasi-singular) are given in Grilli et al. [13], Grilli and Svendsen [17], and Grilli and Subramanya [24,14], for isoparametric and MCI elements.

We now consider the specific implementation of the solution for the two Laplace problems, depending on the type of motion of the submerged body. The body boundary $\Gamma_c(t)$ acts as a moving boundary akin to a wavemaker, within the computational domain Ω, whose motion at each time step is either known from a specified motion or unknown for a freely moving body.

3.1.1. Body in prescribed motion

In this case, Neumann boundary conditions are explicitly specified at each time step, along the body boundary $\Gamma_c(t)$, for both Laplace problems for ϕ and ϕ_t (see, Eqs. (8) and (9)). For each problem, the set of discretized BIEs (Eq. (18)) yields a linear algebraic system of equations of dimension $N\times N$, whose solution (here, using Khaletski's direct elimination technique [13]), provides (ϕ, ϕ_n) and (ϕ_t, ϕ_{tn}) on the entire boundary. Based on these, the free surface position and potential are time-updated to the next time step (this is detailed in the next section). The body boundary position and velocity are then simultaneously time-updated, based on the known prescribed motion.

3.1.2. Freely moving body

In this case, both the position and velocity of nodes on the body boundary $\Gamma_c(t)$ at current time t are assumed to be known from time-updating values from the previous time step. The Neumann boundary condition (8) on $\Gamma_c(t)$ for the first BIEs on (ϕ, ϕ_n) is thus explicitly known, and this first problem is solved as for the prescribed motion case. However, both ϕ_t and ϕ_{tn}, which are required for the Neumann condition of the second BIE for (ϕ_t,ϕ_{tn}), remain unknown along $\Gamma_c(t)$. As detailed in Section 2.4.2, a second BIE (15) is added to the original BIE (18) for (ϕ_t, ϕ_{tn}) so that the number of equations equals the number of unknowns. This new system of BIEs yields an algebraic system of $(N+N_c)$ linear discretized equations with $(N+N_c)$ unknowns, where N_c is the number of nodes on the body boundary $\Gamma_c(t)$. This system is solved using the same direct Khaletski elimination technique. In most cases, for bodies with relatively simple geometry, N_c is no more than 10% of N so that the extra computational cost incurred by solving this larger linear system is quite marginal. As for the case of a prescribed motion, both the free surface position and potential can then be time-updated. This is detailed in the two following sections.

Finally, knowing ϕ_t along $\Gamma_c(t)$ makes it possible computing the pressure p using Eq. (13), which through Eqs. (11) and (12) yields the body center of mass accelerations $\ddot{\boldsymbol{x}}_G$ and $\ddot{\theta}_G$ (taking into account all other externally applied forces and moments). These can be integrated in time to yield the position and velocity of the body boundary nodes at the next time step.

3.2. Time-updating of the free surface geometry and kinematics

Free-surface geometry and potential are explicitly time-updated based on two second-order Taylor series expansions, expressed in terms of a time step Δt and of the successive Lagrangian time derivative D/Dt, of ϕ and $\boldsymbol{r}$ (see, e.g., [13])

$$\boldsymbol{r}(t+\Delta t)=\boldsymbol{r}(t)+\Delta t\frac{D\boldsymbol{r}}{Dt}(t)+\frac{\Delta t^2}{2}\frac{D^2\boldsymbol{r}}{Dt^2}(t)$$

$$\phi(t+\Delta t)=\phi(t)+\Delta t\frac{D\phi}{Dt}(t)+\frac{\Delta t^2}{2}\frac{D^2\phi}{Dt^2}(t) \tag{20}$$

First-order coefficients in these series are identical to the free surface conditions (3) and (4), in which ϕ and ϕ_n are obtained from the solution of the BIE for (ϕ, ϕ_n) at time t. Second-order coefficients are expressed as D/Dt of Eqs. (3) and (4), and calculated using, additionally, the solution of the second BIE for (ϕ_t, ϕ_{tn}), for which boundary conditions are obtained from the solution of the first problem, and also from the treatment of the

submerged body detailed before. Detailed expressions for the Taylor series are given in Grilli et al. [13]. In our simulations, the time step Δt is adjusted at each iteration, depending on an optimal Courant number C_0 (chosen about 0.45 based on [17]) and the minimal distance Δr_{min} between two nodes on the free surface, as

$$\Delta t = C_0 \frac{\Delta r_{min}}{\sqrt{gd}} \tag{21}$$

where d is the local water depth. The accuracy and stability of this explicit scheme was found so high that no filtering or smoothing was needed on the free surface, even after thousands of time steps. More details about the stability and convergence of the time integration scheme of the hydrodynamic solver, as well as a detailed review of 2D applications can be found in [19].

3.3. Time-updating of a freely moving body position and kinematics

To update the position and velocity of the body center of mass to the next time step, Eqs. (11) and (12) are time-integrated based on a Newmark scheme [25], which was retained among a series of methods because of its accuracy and stability. This scheme reads, for the case of Eq. (11)

$$\dot{\boldsymbol{x}}(t+\Delta t) = \dot{\boldsymbol{x}}(t) + \Delta t[(1-\gamma)\ddot{\boldsymbol{x}}(t) + \gamma\ddot{\boldsymbol{x}}(t+\Delta t)]$$

$$\boldsymbol{x}(t+\Delta t) = \boldsymbol{x}(t) + \Delta t\dot{\boldsymbol{x}}(t) + \Delta t^2[(\tfrac{1}{2}-\beta)\ddot{\boldsymbol{x}}(t) + \beta\ddot{\boldsymbol{x}}(t+\Delta t)] \tag{22}$$

where parameters were selected as $\gamma = 1/2$ and $\beta = 1/4$, corresponding to the so-called average acceleration method, which is unconditionally stable for linear systems. As $\ddot{\boldsymbol{x}}(t+\Delta t)$ is unknown, this scheme is implicit and iterations are required. A predictor–corrector loop is used to converge to the value of the hydrodynamic pressure force at the next time step, using as an initial value a fourth-order polynomial extrapolation based on quantities calculated at the five previous time steps. If we define the relative difference between two successive sub-iterations, $i-1$ and i, of the hydrodynamic pressure force $\boldsymbol{F}_p(t+\Delta t)$ at the next time step as

$$\epsilon_{\mathcal{F}}(t) = \left| \frac{\boldsymbol{F}_p^i(t+\Delta t) - \boldsymbol{F}_p^{i-1}(t+\Delta t)}{\boldsymbol{F}_p^{i-1}(t+\Delta t)} \right| \tag{23}$$

a 10^{-6} convergence is generally obtained after two sub-iterations. An example of the required number N_i of sub-iterations for the convergence of the hydrodynamic pressure force will be presented in the next section for a numerical application (see Fig. 8).

4. Energy and volume conservation

In this section, we assess the convergence and accuracy of the 2D-NWT results, for a submerged cylinder in a: (i) forced heaving motion in a water volume initially at rest or (ii) free heaving motion in waves. In case (i) conservation of the fluid volume is checked at each time step, whereas in case (ii) conservation of both cylinder energy and fluid energy, and conservation of fluid volume are checked for the coupled computations detailed above.

4.1. A cylinder in a specified heaving motion

A cylinder of radius $R=0.1$ m is initially submerged at a position $z_c = z_0$ under the free surface at rest, in the middle of a 2D-NWT of depth $d = 10R = 1$ m with lateral reflective vertical walls (Fig. 2). The cylinder is gradually accelerated into periodic heave (i.e., vertical) motion of amplitude $A=R$ and period T, centered on its initial position z_c. The motion of the cylinder generates symmetric waves of wavelength λ, moving in both leftward and rightward directions. The total length of the wave tank is taken to $L = 4\lambda$ with the cylinder located at mid length $x_c = L/2$.

Four cases were successively computed, for two submergence depths $z_0 = -5R = -0.5$ m and $z_0 = -4R = -0.4$ m, and two periods of oscillation $T=0.5$ and 0.8 s, corresponding to linear wavelengths $\lambda = 0.39$ and 1.00 m, respectively, based on the linear dispersion relationship

$$\lambda = \frac{gT^2}{2\pi} \tanh\left(\frac{2\pi d}{\lambda}\right) \tag{24}$$

All simulations were conducted over a duration of 40 periods of oscillation. For a given wavelength, as the mean elevation of the cylinder comes closer to the free surface (z_0 gets closer to zero), the height of generated waves increased and nonlinear effects became more significant. Note that z_0 was kept sufficiently low to prevent waves from overturning over the cylinder and the cylinder from piercing the free surface. Regridding to equal node spacing on the free surface only was applied at every time step.

Fig. 3 first shows the computed free surface elevation at two numerical gages located at horizontal distances $x_g = 2\lambda/3$ and $4\lambda/3$ from the axis of the cylinder (Fig. 2), for two submergence depths of the cylinder, and the period $T=0.5$ s. Symmetric waves generated by the cylinder propagate towards each extremity of the tank. After reflection on sidewalls, reflected and incident waves interact, resulting in a growing wave amplitude in some

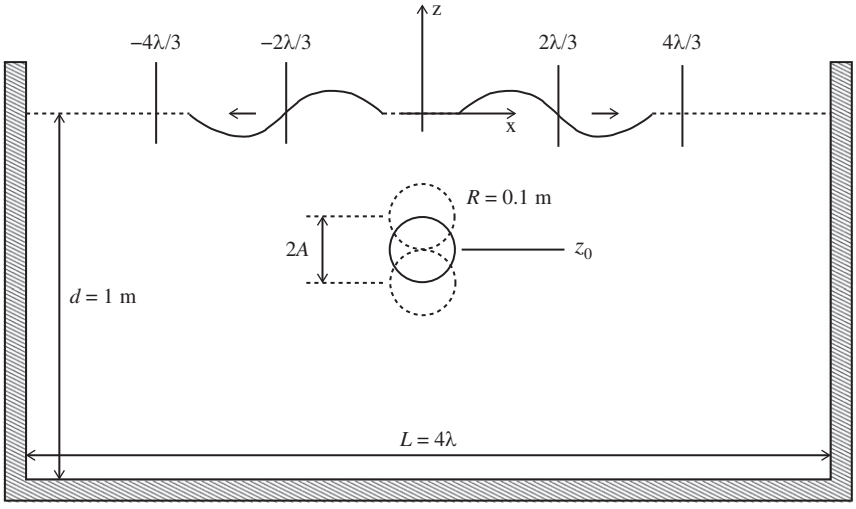

Fig. 2. Sketch of problem geometry for a cylinder of radius $R=0.1$ m in forced heaving motion of amplitude $A=R$ and period T, in water of depth $d=1$ m (not at scale).

local areas of the tank, as clearly seen in Fig. 3 showing the wave records at both gages. As expected, nonlinear effects become more important when the cylinder is closer to the free surface ($z_0 = -0.4$ m). The local wave steepness is defined as H/λ, H being the difference between two successive maximum and minimum of the position of the free surface at a defined location. For instance, steepness at the gages grows from 1.7% after 6 periods of oscillation to 5.1% after 35 periods of oscillation, for $z_0 = -0.4$ m.

The effect of the free surface spatial discretization step Δx on volume conservation is assessed next. Considering an initial fluid volume V_0, the instantaneous relative absolute error on volume conservation is defined as

$$\epsilon_v(t) = \frac{|V(t) - V_0|}{V_0} \tag{25}$$

Fig. 4 shows numerical results for each of the four cases, when successively using a number of BEM nodes per wavelength on the free surface $\Gamma_f(t)$: $N_f = \lambda/\Delta x = 15, 25, 50, 75$, from coarse to fine. We see that the volume error slightly grows with time in each computation, but its maximum value stays at an acceptable level, of less than 0.01%, in all cases for $T=0.5$ s and for the two finest discretization steps for $T=0.8$ s. Fig. 5 summarizes these results by plotting the mean volume error of Fig. 4, after 40 periods of heave oscillations, as a function of the nondimensional spatial discretization step on the free surface. Each curve in the figure has a slope of about 2.7, which shows that convergence of results with spatial discretization is nearly third-order.

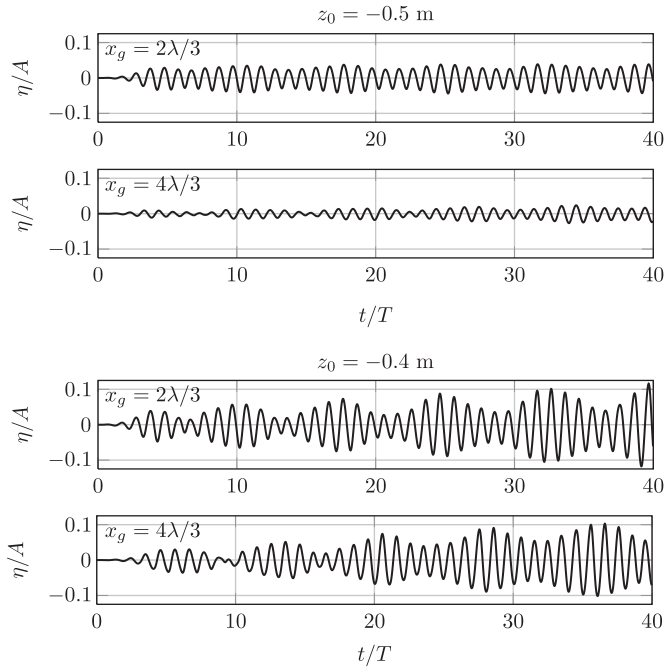

Fig. 3. Case of Fig. 2. Nondimensional free surface elevation (with respect to the amplitude of oscillation A of the cylinder) as a function of nondimensional time, computed at numerical gages located at $x_g = 2\lambda/3$ and $4\lambda/3$ from the cylinder, for two submergence depths z_0 of the cylinder: -0.5 m and -0.4 m. The forced heave amplitude is $A=0.1$ and period $T=0.5$ s.

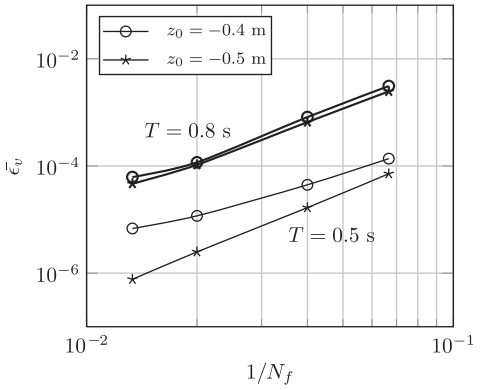

Fig. 5. Case of Fig. 2. Mean volume error after 40 periods of heave oscillation, for $T=0.5$ s and $T=0.8$ s and two cylinder submergence depths, as a function of the nondimensional discretization step $1/N_f = \Delta x/\lambda$.

4.2. A freely heaving cylinder

As sketched in Fig. 6, we now consider a neutrally buoyant cylinder of radius $R=0.1$ m and mass $M = \rho\pi R^2$ per unit length, anchored to the bottom of the tank by a vertical spring of stiffness k_0, which is chosen so that the cylinder oscillation period is $T=1.125$ s. The water depth is $d = 10R = 1$ m. The cylinder can

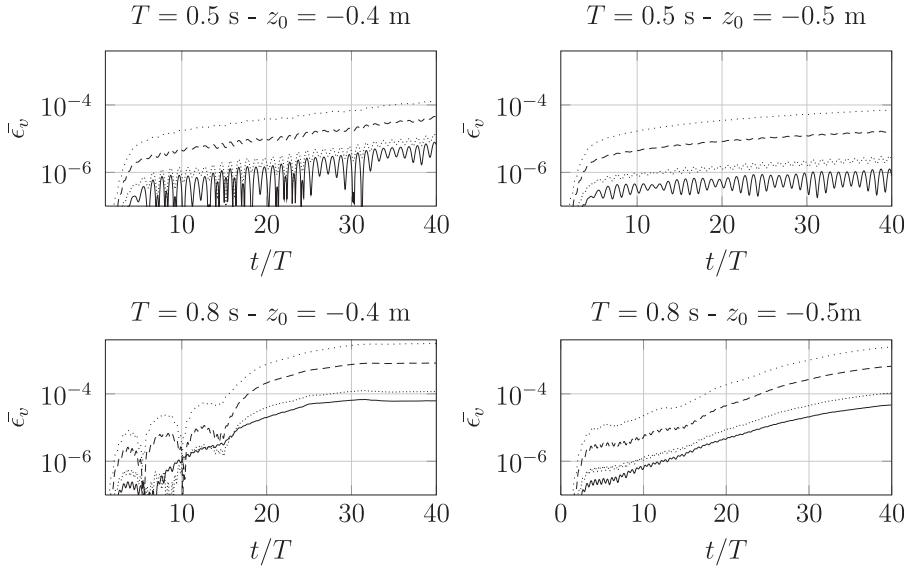

Fig. 4. Case of Fig. 2. Error on volume conservation in the computational domain Ω, for two cylinder submergence depths z_0 and two periods of oscillation T. For each case, results for four spatial free surface discretization steps $\Delta x = \lambda/N_f$ are plotted: $N_f=15$ (···), $N_f=25$ (- - -), $N_f=50$ (...), $N_f=75$ (—).

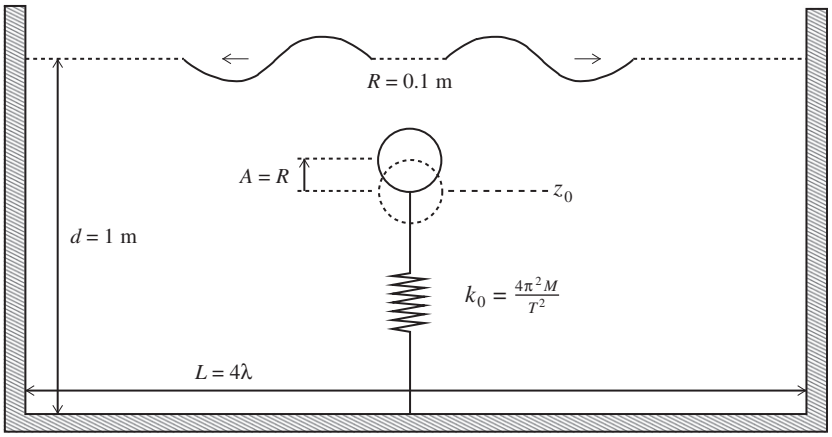

Fig. 6. Sketch of problem geometry for a freely heaving cylinder of radius $R=0.1$ m, following an initial vertical displacement $A=R$, in water of depth $d=1$ m. The cylinder is anchored to the bottom of the tank by a spring of stiffness k_0 (not at scale).

only move vertically and has its initial equilibrium position at depth z_{eq} under the free surface at rest. Spring extension is zero at the equilibrium position of the cylinder z_{eq}. The length of the tank is set to $L=4$ m, similar to the previous problem of forced motion.

At $t=0$, the cylinder is pulled up from its equilibrium position by a distance $A=R$, and released with a zero initial velocity. The cylinder then freely oscillates vertically in heave, around z_{eq}, under the combined action of the hydrodynamic forces from generated waves and of the spring restoring force. Upon release the initial elastic energy of the cylinder/spring system is gradually transferred to the wave motion caused by the cylinder oscillations; the cylinder initially generates symmetric waves, which propagate in both directions away from the cylinder. After reflecting off the sidewalls and propagating back to the cylinder location, these waves transfer part of their energy back to the cylinder.

In the following, to assess the accuracy and convergence of computational results, we derive two energy balance equations, one for the cylinder and one for the surrounding fluid. We first define the body mechanical energy $E_c(t)$ as the sum of its elastic and kinetic energy

$$E_c(t)=\tfrac{1}{2}\,k_0(z_c(t)-z_{eq})^2+\tfrac{1}{2}M\dot{z}_c(t)^2 \tag{26}$$

where z_c stands for the elevation of the center of mass of the cylinder. Due to the neutral buoyancy of the cylinder, its weight is balanced by the hydrostatic pressure force throughout its motion, and the variation of potential energy of the cylinder is well balanced by the work of the vertical hydrostatic pressure force. As a consequence, the variation of body mechanical energy is only due to the work of the vertical hydrodynamic pressure force. Hence, the body energy balance equation reads as

$$\Delta E_c(t)=W(t) \tag{27}$$

where $\Delta E_c(t)=E_c(t)-E_c(0)$ is the mechanical body energy variation with respect to the initial instant, and $E_c(0)=\frac{1}{2}k_0A^2$ is the initial cylinder elastic energy. $W(t)$ is the work of the vertical hydrodynamic pressure force F_z from the initial instant, which writes

$$W(t)=\int_0^t F_z\dot{z}_c\,\mathrm{d}t \tag{28}$$

The fluid mechanical energy is expressed as the sum of its potential and kinetic energy

$$E_f(t)=\frac{1}{2}\rho g\int_{\Gamma(t)}(z+d)^2\,ds+\frac{1}{2}\rho\int_{\Gamma(t)}\phi\frac{\partial\phi}{\partial n}\,ds \tag{29}$$

Similar to the cylinder mechanical energy variation (Eq. (27)), the fluid mechanical energy, as defined by Eq. (29), varies with the work done by the cylinder on the fluid, which reads as

$$\Delta E_f(t)=-W(t) \tag{30}$$

with $\Delta E_f(t)=E_f(t)-E_f(0)$. We numerically verify these two energy conservation principles (Eqs. (27) and (30)) by considering two cases, with equilibrium depths $z_{eq}=-4R=-0.4$ m and $z_{eq}=-3R=-0.3$ m. Denoting $E_{c0}=E_c(t=0)$ the body initial energy, and $E_{f0}=E_f(t=0)$ the fluid initial energy just before releasing the cylinder, the relative errors ϵ_{ec} and ϵ_{ef} on body and fluid energy conservation, respectively, are expressed as

$$\epsilon_{ec}(t)=\frac{\Delta E_c(t)-W}{E_{c0}} \tag{31}$$

$$\epsilon_{ef}(t)=\frac{\Delta E_f(t)+W}{E_{f0}} \tag{32}$$

The relative error ϵ_v on fluid volume conservation is also defined here as

$$\epsilon_v(t)=\frac{V(t)-V_0}{V_0} \tag{33}$$

For the two tested submergence depths, Fig. 7 shows time series of the vertical position of the cylinder, the fluid and cylinder mechanical energy variations with reference to their initial values at $t=0$, the relative errors in cylinder energy conservation and in fluid energy conservation, as a function of nondimensional time t/T. Based on these results, we can summarize the cylinder behavior as follows. Given its initial energy, upon release, the cylinder first oscillates in heave around its equilibrium depth, up to $t/T\approx 7$ for $z_{eq}=-0.4$ m and $t/T\approx 5$ for $z_{eq}=-0.3$ m. During this time, a transfer of energy occurs from the cylinder to the fluid, as seen in Fig. 7 in both the increasing fluid energy and decreasing cylinder energy. This is the time interval during which symmetric waves are generated, which propagate towards the tank sidewalls. When these waves reflect back to the cylinder, its amplitude of motion starts increasing, up to reaching a value close but slightly lower than its initial amplitude A. This second phase, between $t/T\approx 7$ and $t/T\approx 12$ for $z_{eq}=-0.4$ m, and $t/T\approx 5$ and $t/T\approx 9$ for $z_{eq}=-0.3$ m, corresponds to a transfer of energy from the fluid to the cylinder. A new train of waves is then generated, corresponding to energy being transferred back to the fluid, and so forth. At least four full cycles of this dynamics can be seen in Fig. 7, whose periodicity depends on the submergence depth (about $12T$ for $z_{eq}=-0.4$ m and $9T$ for $z_{eq}=-0.3$ m). In both cases, the error on cylinder energy conservation ϵ_{ec} is less than $\sim 0.5\%$, and this error is larger near the maximum amplitude of the cylinder. The error ϵ_{ef} on fluid energy conservation is less than 10^{-5} for $z_{eq}=-0.4$ m and less than 10^{-3} for $z_{eq}=-0.3$ m, due to larger

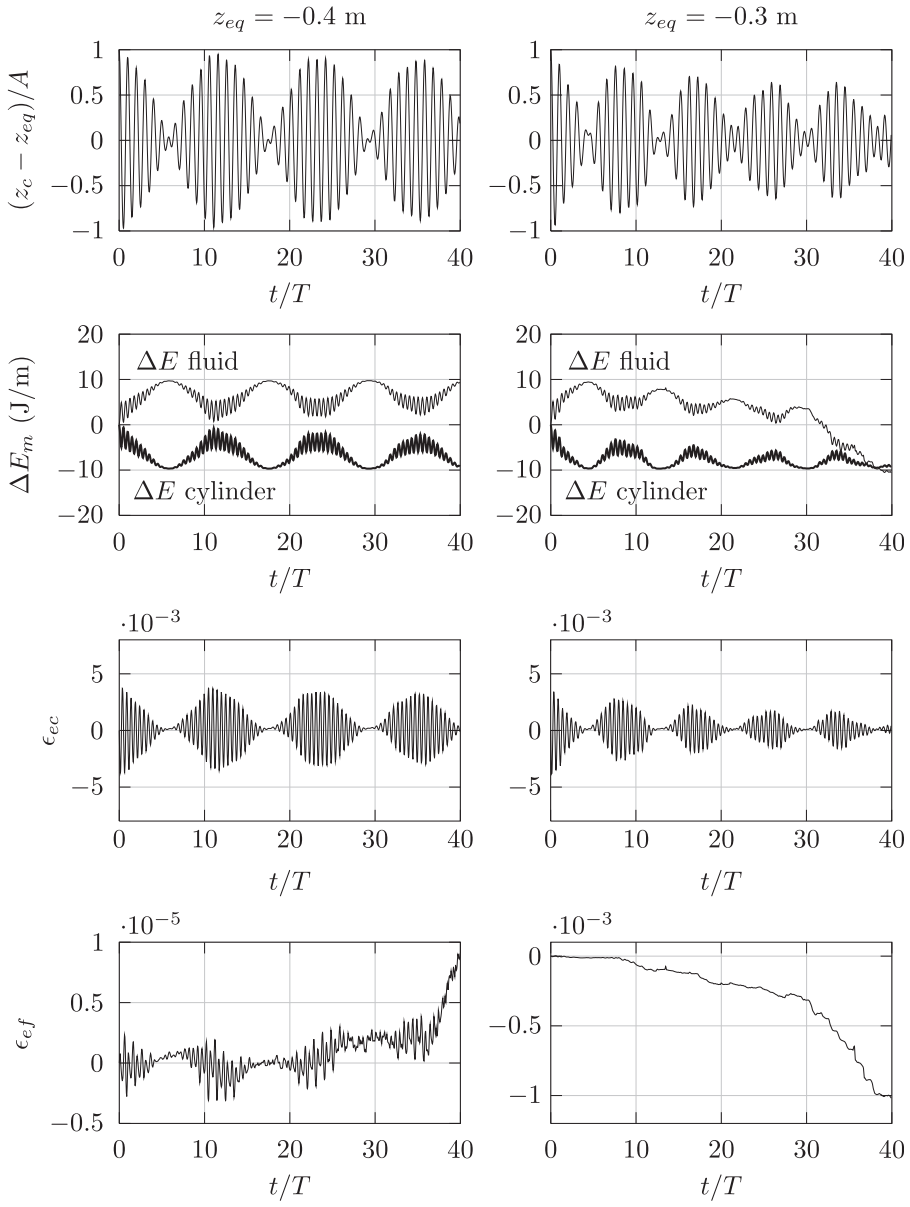

Fig. 7. Time series of nondimensional vertical position of the cylinder from equilibrium depth (upper row), the fluid and cylinder mechanical energy variations from initial instant (second row), the relative error in the cylinder energy conservation (third row) and the relative error in fluid energy conservation (lower row), as a function of nondimensional time t/T. In the BEM, 60 nodes are used on the cylinder boundary and N_f=50 nodes per wavelength on the free surface. Results for the case on Fig. 6, for submergence depth $z_{eq} = -0.4$ m (left column) and $z_{eq} = -0.3$ m (right column).

waves being generated by the cylinder close to the free surface at rest, for the same initial heave amplitude.

Fig. 8 shows, for the same two submergence cases, the number N_i of sub-iterations required to reach convergence in the predictor–corrector loop of the Newmark scheme, used to calculate the hydrodynamic pressure force at the next iteration (see Section 3.3). Convergence is considered to be reached when the relative change between two iterations is less than 10^{-6}. The figure also shows the actual convergence error $\epsilon_{\mathcal{F}}$, which in general is much less than this threshold. Only 1 or 2 sub-iterations are typically needed to achieve convergence.

Finally, Figs. 9 and 10 show time series of cylinder energy, fluid energy and fluid volume conservation errors ϵ_{ec}, ϵ_{ef} and ϵ_v, for three spatial discretization steps on the free surface boundary: N_f=25, 50, 75, and for the two submergence depths of the cylinder. The error ϵ_{ec} on body energy conservation is in phase with the cylinder vertical displacement and is maximum at the highest heave amplitude, while no long-term trend clearly appears. The error ϵ_{ef} on fluid energy conservation seems however to progressively deteriorate with time.

Refining the mesh on the free surface clearly improves both the accuracy of the body dynamics and the accuracy of the flow solution. The figures also show a good correlation between ϵ_{ef} and ϵ_v, which indicates that numerical errors on the fluid part are mainly caused by nonlinear wave effects at the free surface boundary (wave–wave interactions, reflection on sidewalls and potential wave breaking).

5. Comparison with theoretical results

5.1. A submerged cylinder in specified heaving motion

Wu [3] analytically solved the wave radiation problem for a submerged circular cylinder of radius R, in forced heaving motion in still water of infinite depth. The cylinder boundary condition

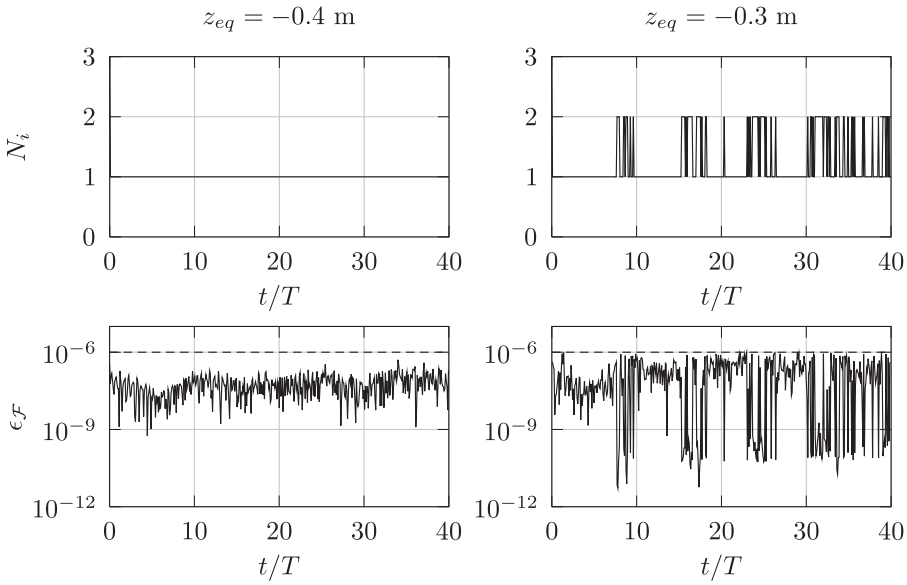

Fig. 8. Time series of the number N_i of sub-iterations required to achieve convergence of the body hydrodynamic pressure force (upper row), and relative error $\epsilon_{\mathcal{F}}$ on the latter at convergence (lower row); the 10^{-6} convergence threshold is marked on the figure (- - -). Results for the case on Fig. 6, for submergence depth $z_{eq} = -0.4$ m (left column) and $z_{eq} = -0.3$ m (right column).

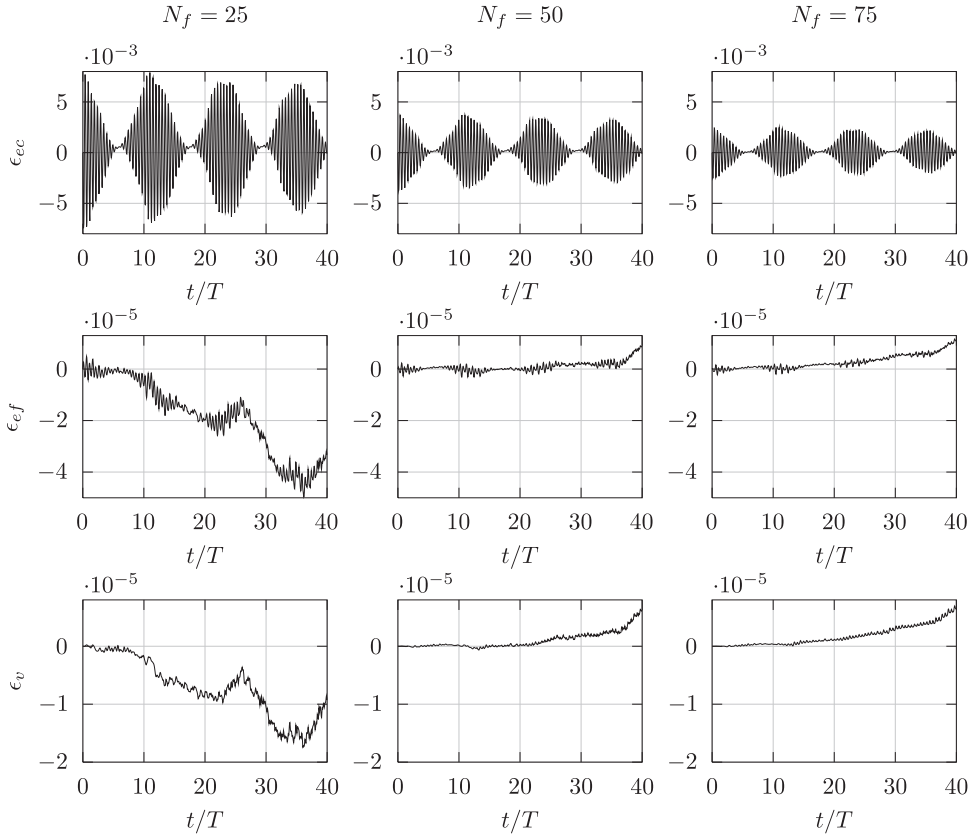

Fig. 9. From top to bottom, time series of cylinder energy error, fluid energy error and fluid volume conservation error. In each column are shown the numerical relative errors for three spatial discretization steps on the free surface boundary: N_f=25 (left column), N_f=50 (central column), and N_f=75 (right column). Results for the case on Fig. 6, for submergence depth $z_{eq} = -0.4$ m.

was satisfied at its instantaneous position, allowing for large amplitude motion, while the free surface conditions were linearized. The wavenumber of generated waves was thus assumed to satisfy the linear dispersion relationship in infinite depth $k = \omega^2/g$. Wu expressed the radiated wave potential as a multipole expansion and computed the vertical hydrodynamic force exerted on the cylinder, assuming a purely vertical motion, for two nondimensional wavenumbers, kR=0.1 and 1.0, and eight nondimensional amplitudes of motion A/R. The nondimensional vertical force was expanded in a Fourier series as

$$\frac{F_z}{\rho A \pi R^2 \omega^2} = F_z^{(0)} + \sum_{n \geq 1} F_z^{(n)} \sin(n\omega t + \psi^{(n)}) \tag{34}$$

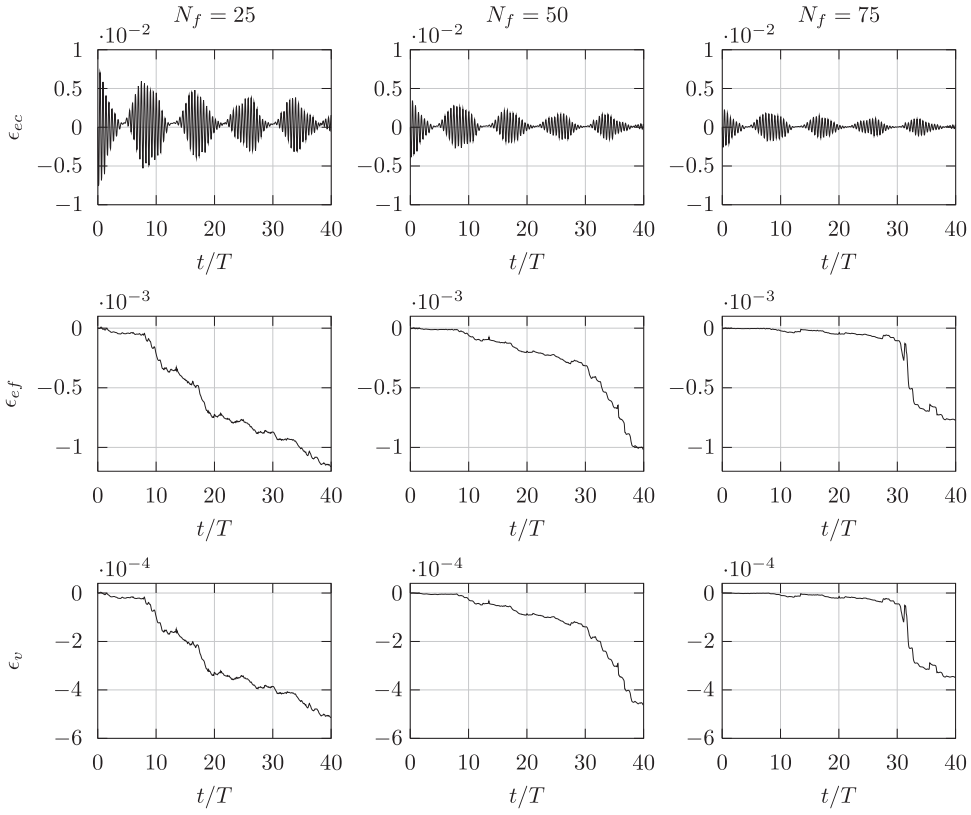

Fig. 10. Similar results as Fig. 9, but for the submergence depth $z_{eq} = -0.3$ m.

We ran numerical simulations for all of Wu's cases, in a NWT of water depth $d=3$ m and length $L=20$ m. A cylinder of radius $R=0.1$ m was placed at mid-length, 10 m away from the leftward boundary, and submerged at $z_c = -3R = -0.3$ m under the undisturbed free surface (mean position). The cylinder was subjected to forced heaving oscillations of angular frequency ω (or period $T = 2\pi/\omega$) and amplitude A. A two period ramp-up was specified to gradually reach steady-state and prevent instabilities that could occur for an impulsive start. Simulations last over a few periods of oscillation and are stopped before reflection appears.

The hypothesis of infinite depth made by Wu was approximately verified in our simulations, for the first frequency of oscillations $kR=0.1$, $k=1\ \mathrm{m}^{-1}$, $T=2.01$ s ($kd = 3 \simeq \pi$) and for the second one $kR=1.0$, $k=10\ \mathrm{m}^{-1}$, $T=0.63$ s ($kd=30$). For both frequencies, 200 nodes were used on the free surface and 80 on the cylinder, in the BEM. Simulations lasted for about 10 periods, starting from a free-surface at rest. In the model, as before, the cylinder motion generated symmetric waves that propagated in both leftward and rightward directions (Fig. 11).

To compare our results with Wu's results, a Fourier transform was applied to the time series of computed vertical pressure force, as defined in Eq. (34), i.e., in nondimensional form, for the last period of simulation. This comparison is shown in Fig. 12, for the zeroth (mean), first, and second harmonics of this force. The agreement with Wu's results is excellent for small amplitudes of motion, but less so for the larger amplitudes. For $A/R > 1$, the cylinder is moving quite close to the free surface and nonlinear effects play a more significant role; hence, Wu's model is expected to be increasingly in error, while our BEM model, which solves FNPF equations, stays accurate throughout. This may explain the discrepancies observed for the larger amplitudes. For the first frequency ($kR=0.1$), the mean vertical force and the first and second harmonics increase with the amplitude of motion. By contrast, for the larger frequency ($kR=1$), only the second harmonic is growing with the amplitude while the mean vertical force is negative, and increasingly so, and the first harmonic is decreasing, with increasing amplitude.

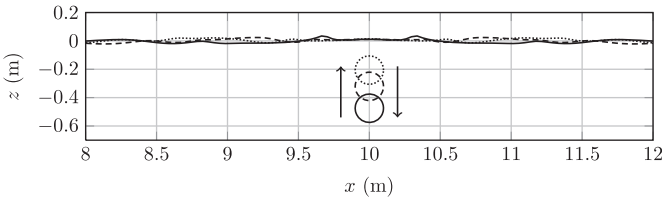

Fig. 11. Forced heaving motion of a cylinder of radius $R=0.1$ m in depth $d=3$ m. Successive snapshots of waves generated at $t/T = 2.75$ (—), 2.99 (- - -), 3.10 ($\cdots$) for an amplitude $A/R = 1.75$, and $kR=0.1$ (period $T=2.01$ s).

5.2. A freely moving submerged cylinder

In Section 4, we verified that provided the BEM discretization is fine enough, very small errors on volume and energy conservation can be achieved, even for long computational times, in situations where the submerged cylinder is freely heaving in the wave tank and waves reflect off the sidewalls. This is a very important result for modeling WECs and accurately predicting the efficiency of WECs undergoing large amplitude motions.

In this section, we study the ability of our model to reproduce the behavior of an idealized WEC: the so-called "Bristol cylinder", introduced and studied in the late 1970s (e.g., [26,27]). This case will serve as a more demanding and realistic test case of our model's predictive capabilities. Thus, we compute the wave-induced motion of a submerged circular cylinder, and compare numerical results to the first-order (linear) solution of Evans et al. [27]. Assuming a mass M per unit length, the wave-induced motion $\boldsymbol{x}$ of the cylinder center of mass, from its initial resting

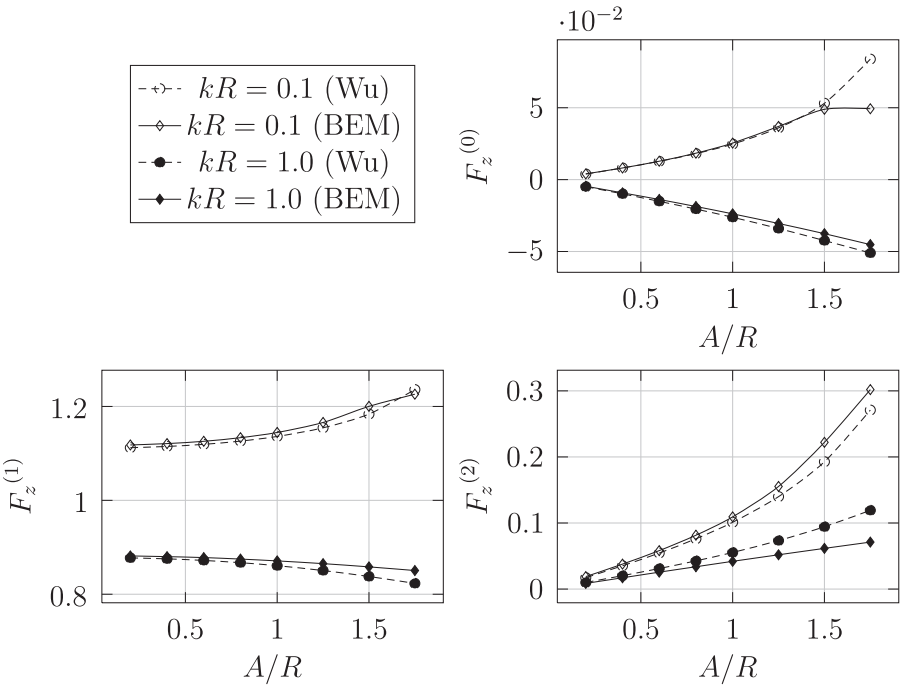

Fig. 12. Case of Fig. 11. Nondimensional zeroth-order (mean), first and second harmonics of the vertical force. BEM/NWT results compared to Wu's semi-linear theory for various amplitudes of body motion A/R and for two frequencies of oscillation ($kR=0.1$ and $kR=1$).

position $\boldsymbol{x}_{ini}$, is governed by

$$M\ddot{\boldsymbol{x}} = \boldsymbol{F}_h + M\boldsymbol{g} - d_0\dot{\boldsymbol{x}} - k_0(\boldsymbol{x}-\boldsymbol{x}_{ini}) \tag{35}$$

where $\boldsymbol{F}_h$ is the wave-induced hydrodynamic force and (k_0, d_0) are the spring stiffness and damping coefficient, respectively, selected identical in the x and z directions, and specified as a function of a "tuning" angular frequency $\omega_0 = 2\pi f_0$ as

$$k_0 = \{M + a_{ii}(\omega_0)\}\omega_0^2 \tag{36}$$

$$d_0 = b_{ii}(\omega_0) \tag{37}$$

with $a_{ii}(\omega_0)$ and $b_{ii}(\omega_0)$ the (linear) added mass and radiative damping, respectively, for the submerged cylinder at the tuning frequency in infinite water depth. Evans et al. showed that, under such conditions and within the linear approximation, the tuned cylinder describes a circle of radius C under the action of regular waves of angular frequency ω and amplitude A

$$\left(\frac{C}{A}\right)^2 = \frac{\rho g^2 b_{ii}(\omega)/\omega}{\{[k_0 - \omega^2(M + a_{ii}(\omega))]^2 + \omega^2(d_0 + b_{ii}(\omega))^2\}} \tag{38}$$

where $a_{ii}(\omega)$ and $b_{ii}(\omega)$ are the (linear) added-mass and radiative damping at frequency ω, respectively.

We simulated one of the configurations studied by Evans et al. [27], namely a neutrally buoyant circular cylinder of radius $R=0.05$ m, whose center is initially at a submergence depth $z_c = -1.25R = -0.0625$ m (i.e., there is $0.75R=1.25$ cm of water above the cylinder). The "tuning" angular frequency is $\omega_0 = 10$ rad/s ($kR=0.51$). To realistically compare model results with Evans et al.'s linear theory, we considered a low wave steepness $H/\lambda = 0.05\%$, and successively ran the model for 12 incident wave frequencies, spread over the interval [0.71 Hz; 2.73 Hz] (ie kR varying from 0.1 to 1.5). The tank depth d was adaptively set for each frequency in order to largely satisfy the infinite depth condition ($kd \approx 25$). An absorbing beach was specified at the end of the tank, over four times the wavelength, to reduce from spurious reflection.

Fig. 13 shows the cylinder trajectory computed for $kR=0.51$ and a small wave steepness $H/\lambda = 0.05\%$. We see that, once steady state is reached, the center of the cylinder describes a stable trajectory around its initial position (corresponding to its equilibrium position). This eventual trajectory is very close to the circular path predicted by the linear theory.

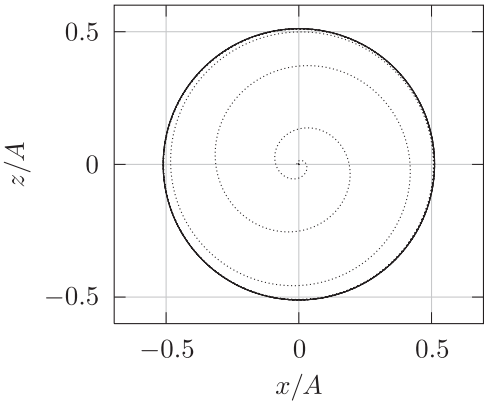

Fig. 13. "Bristol cylinder" case for $H/\lambda = 0.05\%$ and $kR=0.51$. Computed location of the cylinder center as a function of time ($\cdots$), compared to the circular path predicted by Evans et al.'s [27] linear theory (—).

Fig. 14 shows a very good agreement between the mean nondimensional radius of the computed trajectory C/A, as a function of kR, and the prediction of Evans et al.'s linear theory, i.e., Eq. (38).

Unlike in Evans et al.'s linear theory, the cylinder trajectory computed in the NWT is not perfectly circular. Fig. 15 plots the eccentricity e of the trajectory, defined as

$$e = \sqrt{1 - \left(\frac{C_{min}}{C_{max}}\right)^2} \tag{39}$$

where C_{min} and C_{max} are the minimum and maximum amplitudes of the cylinder center trajectory over one period T, respectively. A perfectly circular path would yield a zero eccentricity. As before, the nonlinear NWT results are close to Evans et al.'s zero

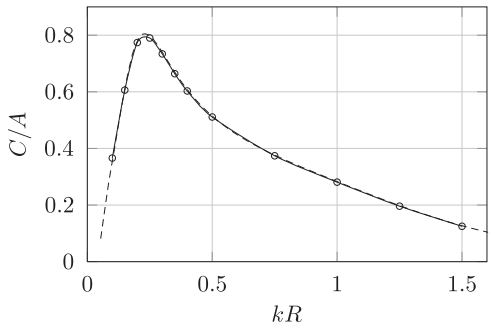

Fig. 14. "Bristol cylinder" case. Mean computed radius of the cylinder trajectory as a function of kR, for a wave amplitude $H/\lambda = 0.05\%$ (–o–) compared to the prediction of Evans et al.'s [27] linear theory (- - -).

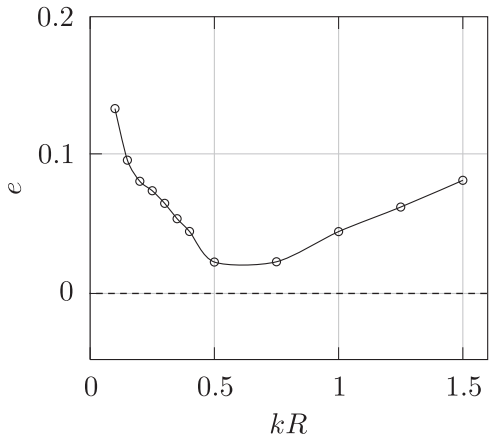

Fig. 15. Same case and symbols as in Fig. 14. Computed eccentricity of the trajectory as a function of kR, for $H/\lambda = 0.05\%$ (–o–), compared to Evans et al.'s [27] linear theory (- - -).

eccentricity for the small value of wave steepness H/λ, without however obtaining a perfectly circular path. In these computations, eccentricity increases as kR decreases and it reaches a maximum of 14% for the lowest simulated frequency (f=0.71 Hz, kR=0.10). This might be due to a lack of resolution on the free surface, simulations with very high resolution being time-consuming, especially for longer waves. Note however that a 14% eccentricity corresponds to a small difference of radii ($C_{min}/C_{max} \approx 0.99$, so, quite close to the expected circular theoretical trajectory). The eccentricity of the trajectory is seen to reach a minimum ($e = 2.1\%$; $C_{min}/C_{max} \approx 0.999$) near the cylinder tuning frequency (kR=0.51).

6. Conclusions

We presented a fully nonlinear numerical model, a 2D-NWT, based on potential flow theory, of wave–body interactions for a submerged body (typically cylindrical). The NWT uses a High-Order Boundary Element Method (HOBEM) to solve for two Laplace problems, for the potential and its time derivative, supplemented by nonlinear free surface boundary conditions. Specific boundary conditions for both problems were presented, with a focus on the submerged body boundary condition, whose expression depends on its type of motion (i.e., prescribed or "free"). In the case of a freely moving body, the fluid–body coupling is based on the *implicit method* proposed by Van Daalen [16], also called the method of the *acceleration potential* by Tanizawa [8]. This method yields an additional Boundary Integral Equation, which expresses the dynamic equilibrium between the fluid and the body. Time updating of the free surface boundary conditions, expressed in a Lagrangian formulation, is based on using two second-order Taylor series expansions, for the potential and the geometry. This scheme is found to be very stable and accurate, and does not require any filtering or smoothing of the free surface. The position and velocity of the body are updated in time using a predictor–corrector algorithm, based on a Newmark scheme with parameters $\gamma = 1/2$ and $\beta = 1/4$ (so-called average acceleration method).

The model accuracy was checked by verifying the fluid volume and energy conservations, for two cases with a heaving submerged cylinder describing large amplitude motions in a tank of limited dimensions. Volume conservation was first checked, for a submerged heaving cylinder in a prescribed motion of large amplitude. Conservation of the cylinder energy and conservation of the fluid energy were then checked, for a freely moving submerged cylinder subjected to a vertical restoring force. In both cases, refining the discretization step between two nodes on the free surface increased the global accuracy of the simulations, which verifies the model convergence. We found that high accuracy could be achieved in the model, with a reasonable discretization. For instance, a free surface discretization of 50 nodes per wavelength with a cylinder immersed at $z_{eq} = -3R$ leads to relative errors of $O(10^{-3})$ on the conservation of cylinder energy, $O(10^{-4})$ on the conservation of fluid energy and $O(10^{-4})$ on the conservation of fluid volume. The fluid energy and volume conservation errors significantly decrease when considering a cylinder submerged deeper under the free surface, due to smaller waves being generated by the cylinder motion.

Numerical results were also compared to analytical formulations based on linear or semi-linear theory for two cases. In the first case, with a submerged horizontal cylinder in forced heaving motion of large amplitude in still water, results agreed well with Wu's semi-linear theory [3]. In the second case, with a freely moving cylinder in waves of low nonlinearity, results agreed very well with Evans et al.'s linear theory [26]. In both cases, as expected, a better agreement was observed between the nonlinear model and the linear theories, for the smallest amplitudes of motion of the cylinder and for waves with low steepness, corresponding to situations where nonlinear effects are moderate to negligible.

References

[1] Mann LD, Burns AR, Ottaviano ME. CETO, a carbon free wave power energy provider of the future. In: Proceedings of the seventh European wave and tidal energy conference (EWTEC), Porto, Portugal; 2007.
[2] Chaplin JF. Nonlinear forces on a horizontal cylinder beneath waves. J Fluid Mech 1984;147:449–64.
[3] Wu GX. Hydrodynamic forces on a submerged circular cylinder undergoing large-amplitude motion. J Fluid Mech 1993;254:41–58.
[4] Cointe R. Quelques aspects de la simulation numérique d'un canal à houle (284p. in French). PhD thesis, Ecole Nationale des Ponts et Chaussées, Paris, France; 1989.
[5] Kent CP, Choi W. An explicit formulation for the evolution of nonlinear surface waves interacting with a submerged body. Int J Numer Methods Fluids 2007;55(11):1019–38.
[6] Koo W, Kim MH. Freely floating-body simulation by a 2D fully nonlinear numerical wave tank. Ocean Eng 2004;31(16):2011–46.
[7] Koo W, Kim MH. Fully nonlinear wave–body interactions with surface-piercing bodies. Ocean Eng 2007;34(7):1000–12.
[8] Tanizawa K. A nonlinear simulation method of 3D body motions in waves (1st report). J Soc Nav Arch Jpn 1995;178:179–91.
[9] Sung HG, Choi HS. Implicit formulation with the boundary element method for nonlinear radiation of water waves. Eng Anal Boundary Elem 2010;34(5):511–29.
[10] Yim SC, Lin H, Robinson DC, Tanizawa K. Predictive capability of a 2D FNPF fluid–structure interaction model. J Offshore Mech Arct Eng 2009;131:1–9.
[11] Tavassoli A, Kim MH. Two-dimensional viscous-flow simulations for a circular cylinder in motion. In: Proceedings of the 10th international offshore and polar engineering conference (ISOPE), Seattle, USA; 2000. p. 478–85.

[12] Tavassoli A, Kim MH. Interactions of fully nonlinear waves with submerged bodies by a 2D viscous NWT. In: Proceedings of the 11th international offshore and polar engineering conference (ISOPE), Stavanger, Norway; 2001. p. 348–54.
[13] Grilli ST, Skourup J, Svendsen IA. An efficient boundary element method for nonlinear water waves. Eng Anal Boundary Elem 1989;6(2):97–107.
[14] Grilli ST, Subramanya R. Numerical modeling of wave breaking induced by fixed or moving boundaries. Comput Mech 1996;17(6):374–91.
[15] Grilli ST, Horrillo J. Numerical generation and absorption of fully nonlinear periodic waves. J Eng Mech 1997;123(10):1060–9.
[16] Van Daalen EFG. Numerical and theoretical studies of water waves and floating bodies. PhD thesis, Universiteit Twente, The Netherlands; 1993.
[17] Grilli ST, Svendsen IA. Corner problems and global accuracy in the boundary element solution of nonlinear wave flows. Eng Anal Boundary Elem 1990;7(4):178–95.
[18] Clément A. Coupling of two absorbing boundary conditions for 2D time-domain simulations of free surface gravity waves. J Comput Phys 1996;126: 139–51.
[19] Grilli ST. Long-wave runup models. Fully nonlinear potential flow models used for long wave runup prediction. World Scientific Publishing; 1997. p. 116–80.
[20] Vinje T, Brevig P. Nonlinear, two-dimensional ship motions. Technical Report of the Norwegian Institute of Technology R-112.81; 1981.
[21] Sen D. Numerical simulation of motions of two-dimensional floating bodies. J Ship Res 1993;37(4):307–30.
[22] Cao Y, Beck RF, Schultz WW. Nonlinear computation of wave loads and motions of floating bodies in incident waves. In: Proceedings of the ninth international workshop on water waves and floating bodies (IWWWFB), Kuju, Fukuoka, Japan; 1994.
[23] Wu GX, Eatock-Taylor R. Transient motion of a floating body in steep water waves. In: Proceedings of the 11th international workshop on water waves and floating bodies (IWWWFB), Hamburg, Germany; 1996.
[24] Grilli ST, Subramanya R. Quasi-singular integrations in the modelling of nonlinear water waves. Eng Anal Boundary Elem 1994;13(2):181–91.
[25] Newmark NM. A method of computation for structural dynamics. J Eng Mech Div, ASCE 1959;85:67–94.
[26] Evans DV. A theory for wave-power absorption by oscillating bodies. J Fluid Mech 1976;77(1):1–25.
[27] Evans DV, Jeffrey DC, Salter SH, Taylor JRM. Submerged cylinder wave energy device: theory and experiment. Appl Ocean Res 1979;1(1):3–12.